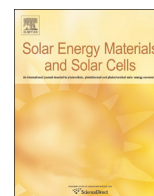




ELSEVIER

Contents lists available at ScienceDirect

Solar Energy Materials & Solar Cells

journal homepage: www.elsevier.com/locate/solmat

One-step-MACE nano/microstructures for high-efficient large-size multicrystalline Si solar cells

Z.G. Huang^{a,b}, X.X. Lin^a, Y. Zeng^a, S.H. Zhong^a, X.M. Song^b, C. Liu^c, X. Yuan^c, W.Z. Shen^{a,*}^a Laboratory of Condensed Matter Spectroscopy and Opto-Electronic Physics, and Key Laboratory of Artificial Structures and Quantum Control (Ministry of Education), Department of Physics and Astronomy, and Institute of Solar Energy, Shanghai Jiao Tong University, Shanghai 200240, People's Republic of China^b School of Science, Huaihai Institute of Technology, Lianyungang 222005, Jiangsu Province, People's Republic of China^c School of Materials Science and Engineering, East China University of Science and Technology, 130 Mei Long Road, Shanghai 200237, People's Republic of China

ARTICLE INFO

Article history:

Received 20 February 2015

Received in revised form

8 July 2015

Accepted 13 July 2015

Keywords:

One-step MACE

Multicrystalline silicon

Nano/microstructures

Large-size

Solar cell.

ABSTRACT

We have employed a one-step (direct etching) metal-assisted chemical etching (MACE) technique to grow large-area Si nanostructures with smoother surface morphology and much less porous Si (PS) defects than those under the two-step (depositing and etching) MACE. A 17.63%-efficiency of the nano/microstructures (N/M-Strus) based multicrystalline Si (mc-Si) solar cells has firstly surpassed that (17.45%) of traditional-micro-textured one with a standard solar wafer size of $156 \times 156 \text{ mm}^2$. The key to success lies in the reduction of electrical loss by removing PS defects and employing shorter one-step-MACE-smoothened N/M-Strus, together with the optical gain from the combined antireflection of mc-Si N/M-Strus and $\text{SiN}_x\text{:H}$ thin films. The present work opens a way to the mass production of high efficient Si nanostructures based solar cells with a less-process-step and lower-cost approach.

© 2015 Elsevier B.V. All rights reserved.

1. Introduction

Vertically aligned silicon (Si) nanostructure arrays have been arising great interests in photovoltaic applications, due to the excellent light-trapping features over a broad range of incident angles [1–3], which may maximize the light absorption and achieve improved efficiency (η) of solar cells. Considering the remaining high reflectance of traditional-micro-textured multicrystalline Si (mc-Si) solar cells, the optical superiority of the Si nanostructures provides an effective approach to obtaining high η of mc-Si solar cells. However, the optical advantage of Si nanostructures has not been facile to be fully converted into the η -gain of solar cells [4–15], which is mainly ascribed to the poor electrical properties, *i.e.*, high recombination on the surface and in the bulk of Si nanostructures. Over the past several years, substantial progresses in improvement of the electric performance have been made by carrying out various process methods such as the surface passivation [16–20], properly increasing sheet resistance [21,22] and optimization of morphology of mc-Si nanostructures [11,13,14,19]. Using the optimized textured structure, Zhong et al., [23] and Xiao et al., [24] have reported η s of 15.99% and 17.46% for

mc-Si nanostructures based solar cells with the standard solar wafer size of $156 \times 156 \text{ mm}^2$ through reactive ion etching (RIE), respectively. Liu et al., [22] have further improved the performance of the mc-Si nanostructures based solar cells by employing acidic-RIE textured technique and high sheet resistance.

As a morphology-easily-controlled method to prepare Si nanostructures, the widely studied metal-assisted chemical etching (MACE) has demonstrated promising advantages for mass productions due to its simplicity, room-temperature process, low cost, and compatibility with current production lines [5,17,19,20]. Generally, MACE is divided into one-step (direct etching) and two-step (depositing and etching) MACE, and the difference between these two methods lies mainly in the less process step and the absence of H_2O_2 (oxidant) for the one-step MACE. Up till now, most of works have focused on two-step MACE, for example, Huang et al., [25] and Lin et al., [26] have reported η s of 11.86% and 15.58% for the mc-Si nanostructures based solar cells through the two-step-MACE technique. Due to the existence of the oxidant H_2O_2 , the Si nanostructures synthesized by the two-step MACE have a mass of porous Si (PS) defects, which is detrimental to the electrical performance of the solar cells. Xie et al., [27] have shown that the Si nanostructures grown by the two-step MACE with lower H_2O_2 concentration have smoother morphology and less PS defects. In short, compared with the two-step MACE, the one-step technique without H_2O_2 is a simpler, less-process-step and lower-

* Corresponding author.

E-mail addresses: yuanxiao@ecust.edu.cn (X. Yuan), wzshen@sjtu.edu.cn (W.Z. Shen).

cost approach to grow large-area Si nanostructures with smoother surface morphology, and thus possesses more promising applications to the mass production of Si nanostructures based solar cells. Using the one-step MACE, Liu et al., [28] have achieved an η of 15.8% on mc-Si nanostructures based $156 \times 156 \text{ mm}^2$ solar cells with a stack passivation of $\text{SiO}_2/\text{SiN}_x$. Hsu et al., [29] have further improved the η to 16.38% for the 6" one-step MACE mc-Si nanostructures based solar cells. Nevertheless, the conversion efficiencies of either the two-step or one-step MACE nanostructured silicon solar cells are still far from satisfactory, especially when compared to the efficiencies of the conventional counterparts.

In this paper, we have successfully fabricated the mc-Si nano/microstructures (N/M-Strus) based solar cells with the standard solar wafer size of $156 \times 156 \text{ mm}^2$, by employing one-step MACE technique. The η of 17.63% is firstly reported to be higher than the traditional-micro-textured one of 17.45%. The shorter one-step-MACE-smoothened N/M-Strus have been proved to play a key role in reducing the electrical loss of N/M-Strus based solar cells, by suppressing the surface recombination, Auger recombination and Shockley–Read–Hall (SRH) recombination. Together with the optical gain from the combined antireflection of the one-step-MACE N/M-Strus and $\text{SiN}_x:\text{H}$ thin films, the reduced electrical loss enables higher-than-traditional-micro-textured η s to be realized. The present achievement of the improved η displays promising future for the mass production of the mc-Si nanostructures based solar cells.

2. Experimental

2.1. Preparation of Si N/M-Strus

p-Type, $200 \pm 10\text{-}\mu\text{m}$ -thick, $\sim 2\text{-}\Omega\text{ cm}$ -resistivity, mc-Si wafers with the standard solar wafer size of $156 \times 156 \text{ mm}^2$ were used for this work. The mc-Si N/M-Strus consisting of the traditional-micro-textures and the nanowires were sequentially prepared in mixed acid solution and MACE solution. The traditional-micro-

textures were firstly prepared in the mixed acid solution $\text{HF}:\text{HNO}_3:\text{DIW}=1:3:2.5$ (volume ratio) for ~ 2.5 min at $\sim 8^\circ\text{C}$. Subsequently, the mc-Si N/M-Strus were synthesized through the MACE including the one-step and two-step process as shown in Fig. 1(a) and (b). For the one-step MACE, the cleaned as-traditional-micro-textured mc-Si wafers were directly etched to form the nanostructures on the surface of the traditional-micro-textures in the etching solution of 4.0 M HF/0.01 M AgNO_3 for a certain time at room temperature. For the two-step MACE, the cleaned as-traditional-micro-textured mc-Si wafers were firstly dripped in the aqueous solution of 5.0 M HF/0.02 M AgNO_3 for 60–100 s to obtain the Ag^+ -deposited layer, and then the Ag^+ -deposited wafers were immediately immersed in the mixed solution of 5.0 M HF and 0.1–1.0 M H_2O_2 for 60 s at room temperature, to form the nanostructures. Finally, to wipe off the residual impurities, all the mc-Si wafers with as-etched N/M-Strus were immersed in the $\text{HNO}_3:\text{DIW}=1:1$ (volume ratio) solution for 20 min, followed by rinsing with excess copious deionized water and drying with N_2 .

2.2. Fabrication of one-step-MACE N/M-Strus based mc-Si solar cells

After the standard RCA cleaning, the mc-Si wafers with one-step-MACE N/M-Strus were placed in a tube furnace to carry out the one-side (double-sides for some wafers) phosphorous diffusion (Meridian, BTU) with POCl_3 liquid source for about 40 min at $\sim 800^\circ\text{C}$. The phosphorous silicate glass (PSG) was removed by a dilute HF solution (9% by volume). After that, the antireflection and passivation layer of $\text{SiN}_x:\text{H}$ was deposited on the front surface by plasma enhanced chemical vapor deposition (PECVD) (E2000 HT410-4, Centrotherm) for ~ 40 min at 400°C , meanwhile the same $\text{SiN}_x:\text{H}$ layers were deposited on both sides of the double-side diffused and no-diffused samples for the purpose of testing the saturation current of the emitter and minority carriers lifetime, respectively. Finally, a conventional front grid pattern and back contacts as well as back surface aluminum were performed by the screen-printing (LTCC, BACCINI), followed by a co-firing step at 750°C for a short duration.

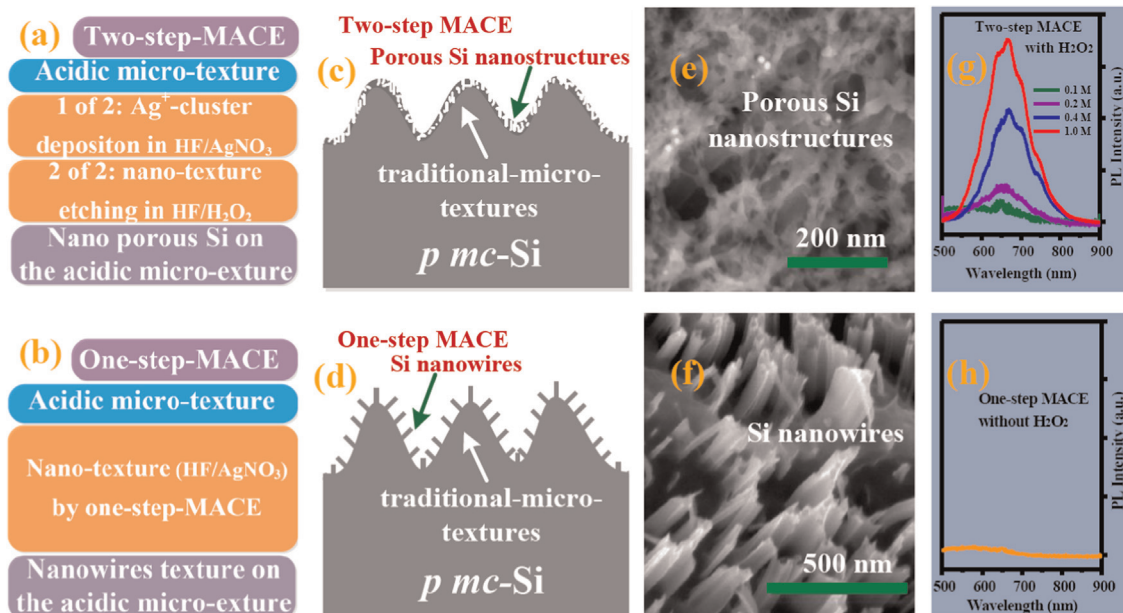


Fig. 1. Comparison between the one-step and two-step MACE. (a) Process flow of two-step MACE. (b) Process flow of one-step MACE. (c) Schematic morphology of the PS nanostructures by the two-step MACE. (d) Schematic morphology of the Si nanowires by the one-step MACE. (e) Oblique-view high-resolution SEM image of PS nanostructures by the two-step MACE. (f) Oblique-view high-resolution SEM image of Si nanowires by the one-step MACE. (g) Room-temperature PL spectra of PS nanostructures by the two-step MACE with different H_2O_2 concentrations of 0.1 M, 0.2 M, 0.4 M and 1.0 M. The excitation wavelength is 325.0 nm. (h) Near zero room-temperature luminescence of Si nanowires by the one-step MACE without H_2O_2 .

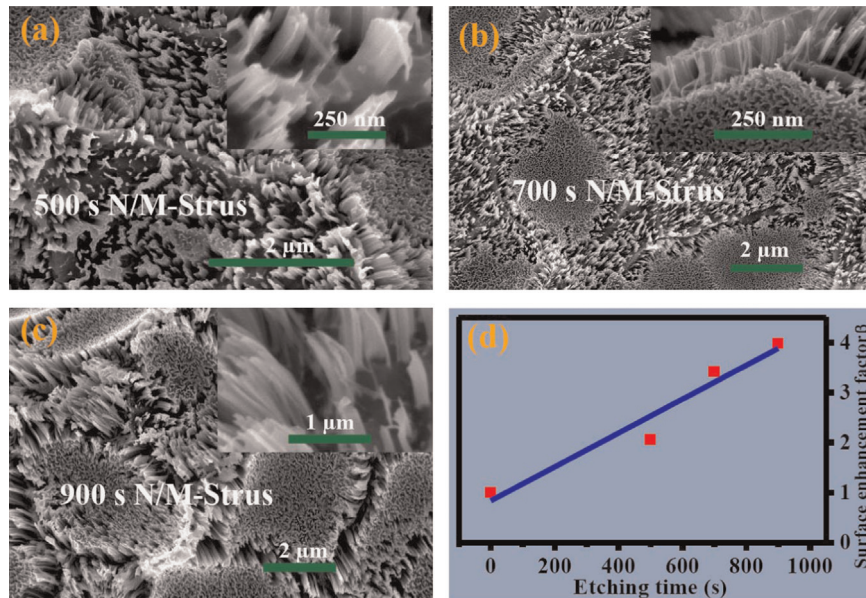


Fig. 2. Smoothed morphology of mc-Si N/M-Strus by one-step-MACE. (a)–(c) Oblique-view SEM images of the one-step-MACE mc-Si N/M-Strus etched for 500, 700 and 900s, respectively, together with the corresponding high-resolution SEM images of the local mc-Si N/M-Strus in the insets. (d) Surface area enhancement factor β with respect to the etching time.

2.3. Characterization

The morphologies of the mc-Si N/M-Strus were investigated by field emission scanning electron microscopy (SEM) (Sirion 200, FEI). The photoluminescence (PL) measurements have been carried out with a micro-Raman system (HR800 UV, Jobin Yvon HORIBA) by using an exciting line of 325.0 nm from a He–Cd laser (IK Series, KIMMON). The reflectance spectra as well as the internal quantum efficiency (IQE) and external quantum efficiency (EQE) were measured on the platform of quantum efficiency measurement (QEX10, PV MEASUREMENTS). The thickness and refractive index of $\text{SiN}_x\text{:H}$ thin film were determined by spectroscopic ellipsometry (SE400, SENTECH). The effective minority carrier lifetimes and the saturation current density of the emitter were obtained by microwave photo-conductance decay method and quasi-steady-state microwave photo-conductance decay method, respectively (WT-1200A, SEMILAB). The electrical parameters of the solar cells were investigated by current–voltage (I – V) measurement under the illumination of AM 1.5 at the Suntech Power Co., Ltd. The performance of the N/M-Strus based mc-Si solar cell with the highest η was independently certified by the TÜV Rheinland (Shanghai) Co., Ltd.

3. Results and discussion

3.1. Smoothed morphology by one-step MACE

Fig. 1 contrastively shows the difference in morphology etched by the one-step and two-step MACE. Fig. 1(c) schematically illustrates that the PS nanostructures are irregularly formed on the surface of the traditional-micro-textured mc-Si by the two-step MACE, while the Si nanowires formed by one-step MACE display smooth and orderly morphology (see Fig. 1(d)). It is worth pointing out that both the nanowires and the traditional acidic texture contribute to the final aspect of the texture. Based on the multi-scale texture (Si N/M-Strus), the shorter nanowires can achieve the same low reflectance, which benefits to the control of the recombination losses [11]. The difference of the morphology is confirmed by the high-resolution SEM images as shown in Fig. 1(e) and (f). From more SEM images of

the PS nanostructures by the two-step MACE, we observe that the thickness of PS layer is enlarged with the increase of the H_2O_2 concentration when the other etching parameters keep the same. According to the fact proved in the Ref. [30], PS generated by anodization or chemical etching in an oxidizing solution ($\text{HF}/\text{H}_2\text{O}_2$), usually give rise to a visible emission. In Fig. 1(g), we present the PL spectra of the PS nanostructures by the two-step MACE with 0.1, 0.2, 0.4 and 1.0 M H_2O_2 . The PL spectra clearly show a broad band emission of 550–850 nm with a peak around 670 nm, which is a characteristic luminescence peak of the mc-Si PS structures [30]. Importantly, the relative PL intensity of PS nanostructures greatly drops with the decrease of the H_2O_2 concentration, and for the 0.0 M series, *i.e.*, the one-step MACE (Fig. 1(h)), the luminescence intensity approaches zero. That means that the nanostructures treated by lower H_2O_2 concentration possess less PS defects, and particularly there is no detectable PS for the 0.0 M H_2O_2 concentration, which is consistent with the previous observation [27]. As we know, PS defects are detrimental to the blue response IQE due to the serious surface recombination [31], which leads to poor output performance of solar cells, especially the open circuit voltage. Consequently, the one-step MACE that produces smoother nanostructures without PS defects is expected to be a more effective way to improve the output performance of mc-Si nanostructures based solar cells.

Next, we focus on studying the influence of the one-step-MACE time on the morphology of N/M-Strus. Fig. 2(a)–(c) shows the SEM images of the one-step-MACE mc-Si N/M-Strus for three series corresponding to 500, 700 and 900s etching time, respectively. Also, the etching velocity at the junctures of micro-textures is larger than that at the bottom of the micro-textures, and thus the nanostructure is general higher at the top of micro-textures than at the bottom. The high-resolution SEM images shown in the insets of Fig. 2(a)–(c) display in detail the morphology of mc-Si nanowires at the junctures of micro-textures: 200 nm-high nanowires with the diameter of ~ 68 nm, 500 nm-high nanowires with the diameter of ~ 60 nm and 670 nm-high nanowires with the diameter of ~ 55 nm, corresponds to the 500, 700 and 900 s series, respectively. As a conclusion, the height of Si nanowires greatly increases with the etching time, while the diameter slightly declines. Since the nanowires on the surface of the traditional-micro-textures lead to a great enhancement of surface area,

we introduce the surface area enhancement factor β to quantitatively characterize the surface area of the N/M-Strus, which is defined as $\beta = A_{N/M}/A_M$ with $A_{N/M}$ being the surface area of the N/M-Strus including the lateral area of all the nanowires and the surface area of the mere traditional-micro-textures A_M [21]. Note that the β is determined by the height, diameter and areal density of the nanowires. Based on the above definition, we have obtained the β values of 2.06, 3.42 and 3.98 for the 500, 700 and 900s series N/M-Strus, respectively, and the β value of the traditional-micro-textures (as reference) is 1.0. Fig. 2(d) depicts the approximately proportional increasing β of the one-step-MACE mc-Si N/M-Strus with respect to the etching time.

3.2. Optical characteristics

Since the optical characteristics of the Si N/M-Strus can directly affect the number of the photons entering into the solar cells [11,20], a good optical performance is the prerequisite to gaining the high η of solar cells. In this section, we lay emphasis on the antireflection characteristics of the one-step-MACE-smoothened N/M-Strus in various conditions including the as-etched, PSG-removed, SiN_x :H-coated and cell cases.

Fig. 3(a) illustrates the influence of the β on the solar averaged reflectance for the one-step-MACE-smoothened N/M-Strus in as-etched, PSG-removed and cell cases. Here, the solar averaged reflectance R_{ave} is calculated by averaging the reflectance over the AM 1.5 spectrum in the wavelength range of 300–1100 nm as follows

$$R_{\text{ave}} = \frac{\int_{300 \text{ nm}}^{1100 \text{ nm}} R(\lambda) \cdot S(\lambda) \cdot d\lambda}{\int_{300 \text{ nm}}^{1100 \text{ nm}} S(\lambda) \cdot d\lambda} \quad (1)$$

where $R(\lambda)$ and $S(\lambda)$ denote the measured reflectance and AM 1.5 solar photon spectral distribution, respectively. Obviously, the as-etched and PSG-removed cases show great drops of R_{ave} with increasing β , while the cell case exhibits slight decline and keeps relatively low R_{ave} s, namely 8.47% ($\beta=1.0$), 7.83% ($\beta=2.06$), 6.40% ($\beta=3.42$) and 5.77% ($\beta=3.98$). Moreover, for the same β , R_{ave} s of

the PSG-removed case are larger than those of the as-etched ones due to the height-reduction of Si nanowires from the alkali corrosion in the PSG-removed process, while R_{ave} s of the cell case have greatly decreased after depositing SiN_x :H layers due to the combined antireflection of one-step-MACE N/M-Strus and SiN_x :H thin films. Note that although the PSG etch affects the morphology of the Si N/M-Strus slightly, the process stability of the Si N/M-Strus based solar cells can be guaranteed due to the stable and fixed PSG etching process.

Fig. 3(b) further manifests the reflectance spectra of the 500, 700 and 900s series for the as-etched case in the wavelength range of 300–1100 nm, together with the traditional-micro-textured series as a reference. It is clear that the reflectance in the whole wavelength range decreases with the increase of the etching time, which can be attributed to the light-trapping effect of the nanostructures in the short wavelength range, and the optical antireflection of the formed density-graded layer in the medium and long wavelength range [32–34].

In order to understand the superiority of the combined antireflection of the N/M-Strus and SiN_x :H, we compare in Fig. 3(c) the reflectance of 500s series with that of the reference (traditional-micro-textured) when the as-etched and the SiN_x :H-coated cases are considered. For the as-etched case, the reflectance of the 500s series is slightly lower than that of reference in the whole range of 300–1100 nm, while for the SiN_x :H-coated case the reflectance difference between the two series has been enlarged in the wavelength ranges of 300–600 nm and 900–1100 nm (highlighted by dashed circles). The enhanced antireflection is attributed to the complementary antireflection effect of the density-graded N/M-Strus at short wavelength and the SiN_x :H thin films at long wavelength [20]. Fig. 3(d) displays the reflectance spectra of the 500, 700, 900s and reference series for the cell case, where the same PECVD process recipe has been used for all cases. We can see that the reflectance spectral curves of the cells with silver grid lines basically keep a similar profile as those of the SiN_x :H-coated case in Fig. 3(c) which has no silver grid lines. Despite a slightly higher reflectance in the medium wavelength range of 500–900 nm, the improved antireflections in the wavelength ranges of

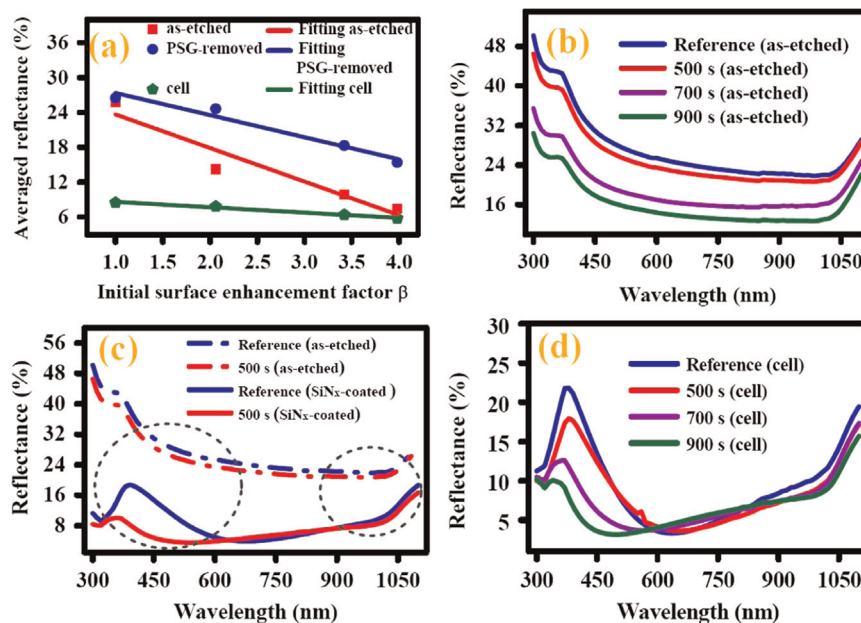


Fig. 3. Reflectance characteristics of the one-step-MACE-smoothened mc-Si N/M-Strus. (a) Solar averaged (300–1100 nm) reflectance with respect to the initial β for the as-etched, PSG-removed and cell cases. (b) Reflectance spectra of the as-etched 500, 700 and 900s series, together with the traditional-micro-textured reference. (c) Comparing the reflectance spectrum of 500s series with that of reference for the as-etched and SiN_x :H-coated cases. (d) Reflectance spectra of the 500, 700 and 900s series for the cell case, together with the traditional-micro-textured reference.

300–600 nm and 900–1100 nm make the solar averaged reflectance reduce with the increase of β , which is expect to benefit the performance of the solar cells [32]. The relationship of the reflectance and theoretical photocurrent is expressed as

$$I_{sc, th} = \int A \frac{e\lambda}{hc} S(\lambda) (1 - R(\lambda)) IQE(\lambda) d\lambda \quad (2)$$

where A and e/hc are the cell area and the charge constant, respectively. Assuming no IQE losses *i.e.* $IQE=1$, the suppression of the reflectance $R(\lambda)$ will be directly beneficial to the improvement of the maximum photocurrent $I_{sc, th}$.

3.3. Electrical analysis

As we know, $SiN_x:H$ thin film by PECVD possesses excellent passivation capabilities, which provides both the good surface passivation from the dangling-bond saturation and bulk passivation from the hydrogen modification [35]. In this section, based on the one-step-MACE-smoothened mc-Si N/M-Strus, we investigate the influence of the morphology on the electrical properties, to deeply understand the electrical loss mechanism of the N/M-Strus based solar cells.

Fig. 4(a) shows the one-step-MACE-smoothened morphology of mc-Si N/M-Strus (500s series) after depositing the $SiN_x:H$ thin film by PECVD, which demonstrates a homogeneous and conformal coating on the surface of the one-step-MACE N/M-Strus. Also, the thickness of the $SiN_x:H$ thin film is estimated as 65.0 nm from the SEM, which is smaller than the 80.0 nm thickness of the traditional-micro-textured series. The reduced thickness of $SiN_x:H$ thin film is due to the constant $SiN_x:H$ -depositing flow on the enhanced surface area of the N/M-Strus, as compared with the traditional-micro-textures. Note that a thin film thickness above 40–50 nm is sufficient to ensure a good surface passivation. In the following, we discuss the recombination mechanisms of the $SiN_x:H$ -passivated N/M-Strus for the doped Si, diffused Si ($p-n$ junction) and mc-Si cell, to understand the nature of the electrical loss in the one-step-MACE N/M-Strus based mc-Si solar cells.

Surface recombination of the Si wafer (thickness d) is usually represented by the effective minority carrier lifetime τ_{eff} , which can be expressed as $1/\tau_{eff} = 1/\tau_{bulk} + (S_{eff}^F + S_{eff}^B)/d$, with τ_{bulk} , S_{eff}^F

and S_{eff}^B being the bulk lifetime, the front and back surface recombination velocity (SRV), respectively. To investigate the effect of the large surface area of Si nanostructures on the SRV, the as-etched nanostructured samples are double-side symmetrically passivated and the SRV is extracted from the measured τ_{eff} based on the following equation [21]

$$\frac{1}{\tau_{eff}} = \frac{1}{\tau_{bulk}} + S_{eff} \frac{2}{d} \quad (3)$$

where $S_{eff} = S_{eff}^F = S_{eff}^B = \beta \cdot S_{loc}^F$. Here the constant S_{loc}^F denotes the local SRV at the front surface of nanostructures (Auger recombination is neglected in the case of non-diffused samples). Fig. 4 (b) shows that τ_{eff} of the one-step-MACE-smoothened N/M-Strus for both the as-etched and $SiN_x:H$ -passivated cases, slightly decrease with increasing β , which is consistent with the previous results [19–21]. Obviously, all the four series for the as-etched case have low values of lifetime, while the $SiN_x:H$ -passivated counterparts possess a lifetime an order of magnitude higher due to the good passivation effect from the $SiN_x:H$ layer. It is worth noting that the $SiN_x:H$ -passivated case shows little lifetime difference among the different series corresponding to $\beta=2.06, 3.42$ and 3.98 , indicating that the good $SiN_x:H$ passivation weakens the adverse influence of the surface area enhancement.

Generally, the saturation current density J_{0e} of the emitter for diffused Si ($p-n$ junction) can characterize the Auger recombination in the emitter and the surface recombination at the surface of the emitter [36]

$$\frac{1}{\tau_{eff}} - \frac{1}{\tau_{Auger}} = \frac{1}{\tau_{SRH}} + \left(J_{0e (front)} + J_{0e (back)} \right) \frac{N_A + \Delta n}{qn_i^2 d} \quad (4)$$

where τ_{Auger} and τ_{SRH} are the Auger recombination and the bulk lifetime considering only the SRH recombination, respectively, N_A is the doping concentration of the p -Si substrate, Δn is the excess carrier density, q is the elementary charge, and n_i is the intrinsic carrier density. Fig. 4(c) shows $1/\tau_{eff} - 1/\tau_{Auger}$ with respect to the excess carrier density Δn for the double-side-diffused and double-side- $SiN_x:H$ -passivated mc-Si N/M-Strus ($J_{0e (front)} = J_{0e (back)}$), where Kerr Auger recombination model [37] is considered. Note that these wafers are passivated by the same $SiN_x:H$ layer as that in

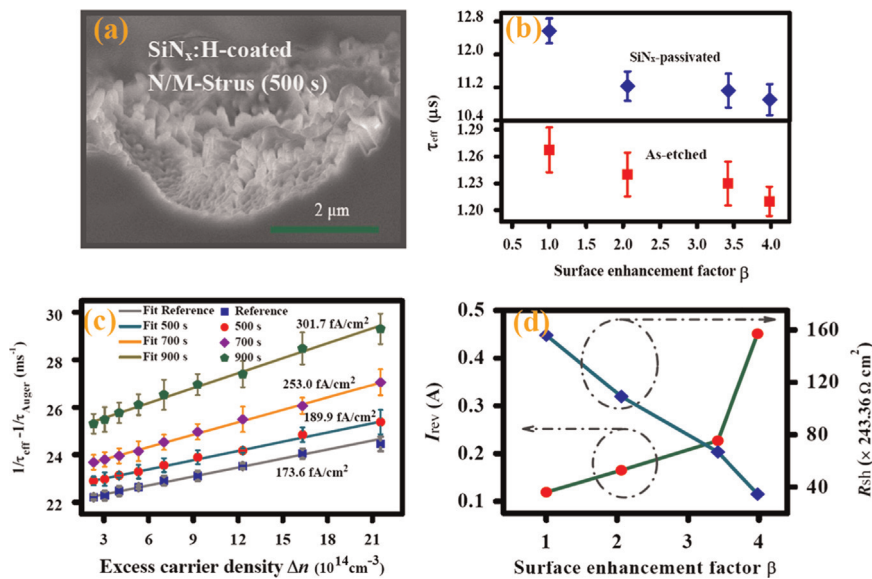


Fig. 4. Electrical characteristics of the one-step-MACE-smoothened mc-Si N/M-Strus passivated by $SiN_x:H$ thin film. (a) Morphology of the $SiN_x:H$ -coated mc-Si N/M-Strus. (b) Effective minority carrier lifetime τ_{eff} with respect to β for the as-etched (lower) and $SiN_x:H$ -passivated (upper) mc-Si N/M-Strus. (c) $1/\tau_{eff} - 1/\tau_{Auger}$ with respect to the excess carrier density Δn for the double-side-diffused and double-side- $SiN_x:H$ -passivated mc-Si N/M-Strus, together with the traditional-micro-textured reference. (d) Reverse saturation current I_{rev} (left) and shunt resistance R_{sh} (right) of the mc-Si N/M-Strus based solar cells with respect to β . The reversed bias voltage is set as -12.0 V.

Section 2.2. According to the extracted slopes, J_{0e} of the 500, 700, 900s and reference (traditional-micro-textured) series are calculated as 189.9, 253.0 and 301.7 and 173.6 fA/cm², respectively, which implies a growing recombination including surface and Auger recombination in the emitter with increasing β .

In view of good passivation of the SiN_x:H layer, J_{0e} represents the dominating Auger recombination and secondary SRH recombination in the heavily doped emitter. Therefore, the larger J_{0e} of the emitter is mainly attributed to the higher Auger recombination produced by the thicker “dead layer” of the heavily doped N/M-Strus with larger β , which is consistent with Refs. [10,18]. Also, we should note that the 500s series ($\beta=2.06$) has almost identical J_{0e} with the reference, demonstrating that the electrical loss in the emitter of 500s series keeps the same level with that of the reference ($\beta=1$), while the electrical performance of the 700s ($\beta=3.42$) and 900s ($\beta=3.98$) series are far poorer than that of the reference. It reveals that the Auger recombination rapidly aggravates with the increase of β , and thus the careful control of the morphology is an important factor to suppress the Auger recombination of the one-step-MACE N/M-Strus based solar cells.

For the Si nanostructures based solar cells, Shen et al., [38] have introduced a lateral electric field of the non-uniform $p-n$ junction to explain the enlarged leakage current and the reduced shunt resistance. In fact, the lateral electric field of the non-uniform $p-n$ junction produces an extra SRH recombination by increasing the capture probability of the electrons and holes, which results in the worsened leakage current and shunt resistance. Therefore, it is necessary to study the influence of the non-uniform morphology of mc-Si N/M-Strus on the leakage current and shunt resistance of the solar cells, which can provide a helpful guidance for the fabrication of the solar cells. Fig. 4(d) illustrates both the reverse saturation current I_{rev} (left) and the shunt resistance R_{sh} (right) with respect to β for the one-step-MACE N/M-Strus based mc-Si solar cells. With the increase of β , i.e., the increasing non-uniformity of the morphology, I_{rev} evidently ascends from 0.165 A of the 500s series to 0.451 A of the 900s series, meanwhile R_{sh} reduces from 26575 Ω cm² of the 500s series to 8415 Ω cm² of 900s series. This shows that the one-step-MACE N/M-Strus based solar cell with larger β possesses larger I_{rev} and smaller R_{sh} , which is partially ascribed to the stronger lateral electric field from the non-uniform $p-n$ junction [38]. Naturally, the worsened I_{rev} and R_{sh} caused by the growing SRH recombination reduce the open circuit voltages of the solar cells, as can be clearly observed in Table 1.

In summary, it is concluded from the above discussion that the surface recombination, Auger recombination and extra SRH recombination have simultaneously become higher with

increasing β , and can be suppressed by employing the shorter one-step-MACE-smoothened N/M-Strus. However, as the discussion in Section 2, the antireflection performance of the higher N/M-Strus (larger β) is superior to that of the shorter ones (smaller β). In a word, a careful tradeoff of the optical gain and electrical loss is the most important step to achieve high η of one-step-MACE N/M-Strus based mc-Si solar cells.

3.4. Cell performance

Measured output parameters of the one-step-MACE N/M-Strus based and traditional-micro-textured (reference) mc-Si solar cells are listed in Table 1. Obviously, the short circuit currents (I_{sc} s) of the one-step-MACE N/M-Strus based solar cells increase with increasing of β , and all of them are higher than that of the reference, which benefits from the combined antireflection performance of the N/M-Strus and SiN_x:H thin films. On the contrary, the open circuit voltages (V_{oc} s) show a declining trend, and all of them are lower than that of the reference, mainly due to the worsened surface recombination and Auger recombination together with the extra recombination from the lateral electric field of the non-uniform $p-n$ junction. Moreover, as discussed in Section 3.3, the shunt resistances (R_{sh} s) and reverse saturation currents (I_{rev} s) are greatly affected by the β , implying that a good electrical performance cell requires shorter one-step-MACE-smoothened N/M-Strus. The series resistances (R_{ser} s) show low values (~ 0.5 Ω cm²) and no evidently changing with increasing β , manifesting a good electrical contact between the front electrode and one-step-MACE N/M-Strus emitter. The good contacts that are beneficial to the fill factor (FF) profit from the enough contact area between the front electrode and the compact Si nanostructures, which has been proved in previous work [25]. In short, the optimal tradeoff between the optical gain and electrical loss has resulted in the best output cell performance in the 500s one-step-MACE N/M-Strus based solar cells with an averaged η up to 17.57%, which is higher by an absolute 0.12% compared with 17.45% of the traditional-micro-textured reference. To illustrate the superiority of one-step-MACE, the averaged performance of two-step-MACE N/M-Strus based solar cells are obtained as follows: $\eta=16.85\%$, $I_{sc}=8.610$ A, $V_{oc}=0.6179$ V, $R_s=0.7593$ Ω cm², $I_{rev}=0.5576$ A. Compared with non-optimized 900s one-step-MACE cells, the averaged η of two-step-MACE cells declines by an absolute 0.4%, although both of them have the similar optical performance. As is discussed in Fig. (1), PS generated by two-step-MACE cause more electrical loss including lower V_{oc} , larger I_{rev} and R_s , which is related to more recombination loss and poorer electrical contact. Considering a low additional cost of one-step-MACE method, we believe that the

Table 1

Experimental and simulated (PC1D) results of the one-step-MACE N/M-Strus based and traditional-micro-textured (reference) mc-Si solar cells with the standard solar wafer size of 156 × 156 mm². These ISO certified output parameters (AM 1.5 illumination) are measured at the Suntech Power Co., Ltd. Basic parameters of PC1D-simulation are set as follows: background doping concentration, n -type emitter doping concentration, p -type mc-Si bulk minority carrier lifetime and base contact are 2.65×10^{16} cm⁻³, 8.23×10^{19} cm⁻³, 50.0 μ s and 1.90×10^{-3} Ω , respectively. Note that all the basic parameters are experimental obtained from data of the production line which guarantees the reliability of the fitting results. The theoretical maximums of $I_{sc,th}$ and η are calculated by the Eq. (2) and $\eta=I_{sc,th}V_{oc}FF/P_{in}$.

Cell (156 × 156 mm ²)	Experimental								R_{ave} (%)	Simulated		Theoretical maximum	
	I_{sc} (A)	V_{oc} (V)	FF (%)	η (%)	I_{rev} (A)	R_{ser} (Ω cm ²)	R_{sh} (Ω cm ²)	Sheet Resistance (Ω sq ⁻¹)		DL (nm)	η (%)	$I_{sc,th}$ (A)	η_{th} (%)
500s N/M-Strus	8.5839	0.6258	79.59	17.57	0.165	0.4794	26575	81	7.83	120.0	17.65	9.715	19.84
700s N/M-Strus	8.5924	0.6244	79.62	17.45	0.227	0.4648	16269	75	6.40	152.0	17.38	9.807	20.03
900s N/M-Strus	8.5954	0.6223	79.07	17.22	0.451	0.4721	8415	70	5.77	170.0	17.23	9.856	20.13
Reference	8.5526	0.6261	79.26	17.45	0.119	0.5037	37964	85	8.47	101.0	17.47	9.644	19.70

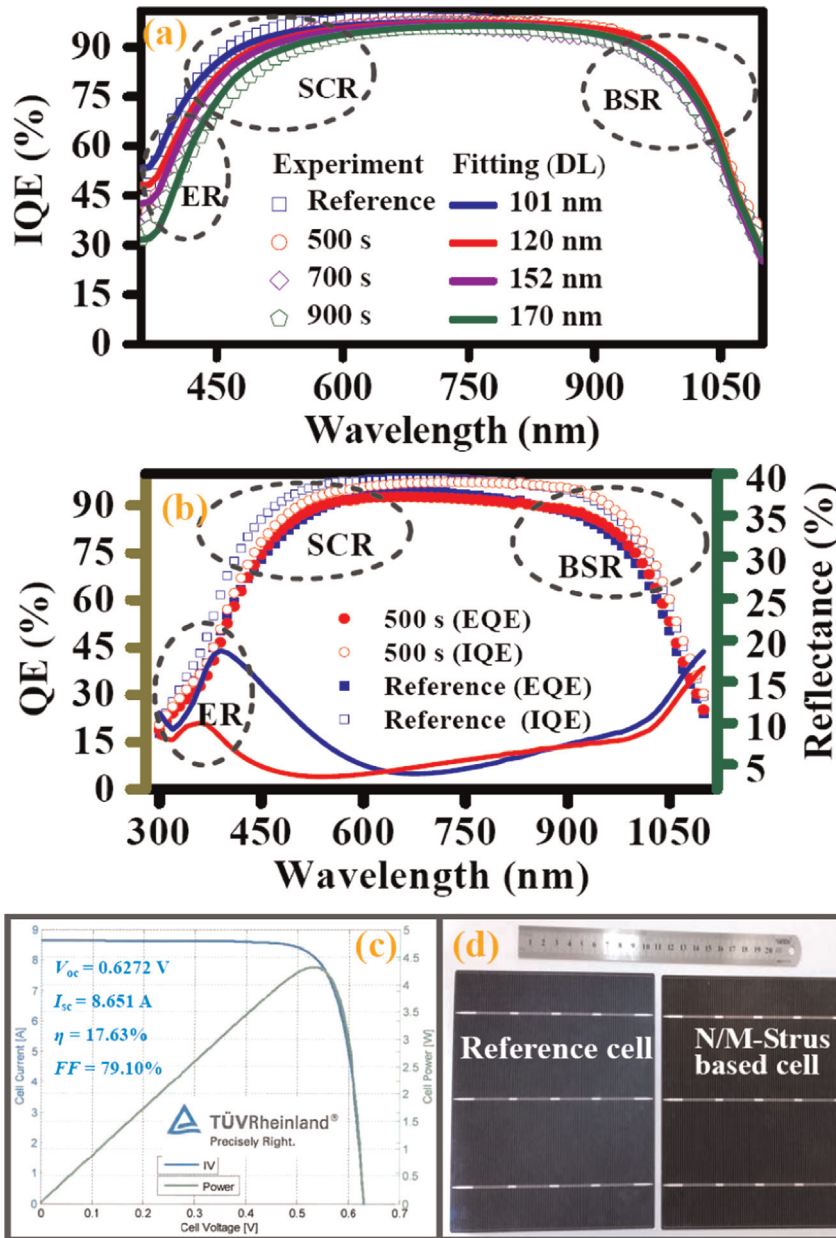


Fig. 5. Cell performance of the one-step-MACE N/M-Strus based mc-Si solar cells. (a) Experimental (hollow symbols) and PC1D-fitting (solid curves) IQE, together with the traditional-micro-textured reference. (b) Comparing IQE, EQE and reflectance of the 500s one-step-MACE N/M-Strus based solar cell with those of the traditional-micro-textured reference. (c) Output parameters, current-voltage (blue curve) and power-voltage (green curve) characteristics of the highest-efficient one-step-MACE N/M-Strus based mc-Si solar cell (500s series) independently certified by the TÜV Rheinland (Shanghai) Co., Ltd. (d) Photograph of the one-step-MACE N/M-Strus based and traditional-micro-textured (reference) mc-Si solar cells with the standard solar wafer size of 156×156 mm². (For interpretation of the references to color in this figure legend, the reader is referred to the web version of this article.)

one-step-MACE method is a cost-effective technique to promote the η of multicrystalline solar cells and promising to be applied to mass production.

To further understand the influence of the morphology on the IQE, we have measured the IQEs (hollow symbols) of the one-step-MACE N/M-Strus based and the reference mc-Si solar cells, and simulated the corresponding ones (solid curves) by PC1D software as shown in Fig. 5(a). Generally, the total IQE is regarded as the sum of the following three contributions [39]:

$$IQE = IQE_{ER} + IQE_{SCR} + IQE_{BSR} \quad (5)$$

where IQE_{ER} , IQE_{SCR} and IQE_{BSR} denote the IQE in the emitter region (ER), space charge region (SCR) and back surface region (BSR), respectively.

Different recombination mechanism dominates in different regions, e.g., the surface and Auger recombination in ER, SRH recombination in SCR, and back surface recombination in BSR. As highlighted by dashed circles in the figure, the measured IQE in ER (the short wavelength range) and SCR (the medium wavelength range) decrease with the increasing β , while they exhibit similar behaviors in BSR (the long wavelength range).

Firstly, the worsening IQE in ER with increasing β can be regarded as the contribution of a “dead layer” (DL) from the heavily doped Si emitter, which has been proved in Refs. [10,18]. To illustrate this, we have employed the PC1D software to simulate the IQE with the detailed parameter setting listed in the caption of Table 1. The reliability of the simulation is guaranteed by extracting the basic input parameters from the actual production-

line data and proved by the matching between the simulated η (see simulated part of Table 1) and the experimental ones. To match the fitting IQE curves with the experimental ones, the values of the DL thickness should be set as 120.0, 152.0 and 170.0 nm corresponding to the reference, 500, 700 and 900s series, respectively, which is consistent with the experimental result of the lower sheet resistance with the larger β . That is to say, the more electrical loss from the surface and Auger recombination at/in ER can be attributed to the existence of a thicker DL (larger β). Secondly, in SCR, the SRH recombination produced by the non-uniform p - n junction enlarges with increasing β , which leads to the declining IQE, in good agreement with the result of Section 3.3. Finally, the IQE in BSR is kept in the same level for all the series simply due to the same cell process in this region. In brief, the shorter one-step-MACE N/M-Strus based solar cells possess better IQE in ER and SCR due to the lower surface, Auger and SRH recombination losses, while all the series basically keep the same level of IQE in BSR. Assuming no IQE loss, the theoretical maximums of $I_{sc,th}$ and η_{th} are predicted in Table 1. With the increase of the β , the experimental I_{sc} shows the same increasing trend with that of the theoretical $I_{sc,th}(\eta_{th})$, while the experimental η s decrease due to the rapidly deteriorated IQEs.

From the measured IQE, EQE and reflectance, Fig. 5(b) clearly illustrates the tradeoff between the optical gain and electrical loss by comparing the 500s one-step-MACE N/M-Strus based solar cell with the traditional-micro-textured reference. Although the 500s series shows poorer IQE than the reference in ER and SCR, the EQE keeps the same level in ER and better one in SCR, thanks to the excellent optical gain in the corresponding wavelength range. Furthermore, the superior optical performance of the 500s series in the long wavelength range promotes the EQE in BSR, since the 500s series has the same level IQE as the reference in this region. As a result, the 500s series yield higher η s than the traditional-micro-textured ones, benefiting from the improvement of the EQE due to the optical gain from the combined antireflection and the control of the electrical loss. Among the optimal 500s one-step-MACE N/M-Strus based solar cells, the highest η of 17.63%, as well as $I_{sc}=8.6510$ A ($J_{sc}=35.56$ mA/cm²), $V_{oc}=0.6272$ V and $FF=79.10\%$, has been independently confirmed by TÜV Rheinland (Shanghai) Co., Ltd. (see Fig. 5(c)). Fig. 5(d) displays the photograph of the one-step-MACE N/M-Strus based mc-Si solar cell with black appearance and standard solar wafer size of 156×156 mm² (right), together with the traditional-micro-textured reference cell (left). Although the process was performed on a standard solar wafer size of 156×156 mm², the appearance of the Si N/M-Strus based solar cell looks uniform across the wafer.

4. Conclusions

In conclusion, we prepare the mc-Si nanostructures on the acidic micro-texture by the one-step and two-step MACE, and contrastively investigate the process flow, morphologies and PL spectra of them. The room-temperature PL measurement proves that the one-step MACE is superior to the two-step MACE, due to smoother and more orderly mc-Si nanostructures without detectable PS defects. Therefore, one-step-MACE N/M-Strus based mc-Si solar cells are fabricated on the standard solar wafer size of 156×156 mm² by using commercial screen-printed technique. The study of the optical characteristics shows that with the increase of the nanowire height (proportional to the etching time), the averaged reflection R_{ave} s become lower, especially in the short wavelength region. Although the R_{ave} reduction of the higher N/M-Strus implies the improvement of the photocurrent, the electrical analysis manifests that the higher N/M-Strus based mc-Si solar cell suffers from the larger electrical losses from the surface recombination, Auger recombination and extra SRH recombination, and

thus the shorter one-step-MACE N/M-Strus is more beneficial to controlling the electrical loss. Also, the worsening electrical performances with the increase of the height are confirmed by the experimental IQE and its simulation by PC1D. The trade-off of the optical gain and the electrical loss is found in 500s case that possesses higher I_{sc} , similar V_{oc} and FF (fill factor), comparing with those of the traditional-micro-textured solar cell. Furthermore, the EQEs improvements of 500s case in the short wavelength and long wavelength region confirm the aforementioned optical and electrical results. Finally, we successfully achieved the highest η of 17.63% (confirmed by the TÜV Rheinland Co., Ltd.) and the average η of 17.57% for the mc-Si N/M-Strus based solar cell, surpassing 17.45% of the reference (traditional-micro-textured) counterparts. By employing the simple and low-cost one-step MACE technique, the realization of improved η on the mc-Si N/M-Strus based solar cells with standard solar wafer size will strongly drive the research development and mass production of high efficient Si nanostructures based solar cells.

Acknowledgements

This work was supported by the National Natural Science Foundation of China (11174202, 61234005 and 11474201), Shanghai Municipal Project (14DZ1201000), the Natural Science Foundation of Jiangsu Province (BK20140448) and the Innovation Foundation of HHIT (Z2014018).

References

- [1] S. Koynov, M.S. Brandt, M. Stutzmann, Black nonreflecting silicon surfaces for solar cells, *Appl. Phys. Lett.* 88 (2006) 203107.
- [2] H.M. Branz, V.E. Yost, S. Ward, K.M. Jones, B. To, P. Stradins, Nanostructured black silicon and the optical reflectance of graded-density surfaces, *Appl. Phys. Lett.* 94 (2009) 231121.
- [3] X.G. Liu, P.R. Coxon, M. Peters, B. Hoex, J.M. Cole, D.J. Fray, Black silicon: fabrication methods, properties and solar energy applications, *Energy Environ. Sci.* 7 (2014) 3223.
- [4] B.M. Kayes, H.A. Atwater, N.S. Lewis, Comparison of the device physics principles of planar and radial p - n junction nanorod solar cells, *J. Appl. Phys.* 97 (2005) 114302.
- [5] K.Q. Peng, Y. Xu, Y. Wu, Y.J. Yan, S.T. Lee, J. Zhu, Aligned single-crystalline Si nanowire arrays for photovoltaic applications, *Small* 1 (2005) 1062.
- [6] Q. Shu, J. Wei, K. Wang, H. Zhu, Z. Li, Y. Jia, X. Gui, N. Guo, X. Li, C. Ma, D. Wu, Fabrication of slantingly-aligned silicon nanowire arrays for solar cell application, *Nanotechnology* 19 (2008) 255703.
- [7] M. Naughton, K. Kempa, Z. Ren, Y. Gao, J. Rybczynski, N. Argenti, W. Gao, Y. Wang, Y. Peng, J. Naughton, G. McMahon, T. Paudel, Y. Lan, M. Burns, A. Shepard, M. Clary, C. Ballif, F. Haug, T. Söderström, O. Cubero, C. Eminian, Hybrid heterojunction and photoelectrochemistry solar cell based on silicon nanowires and double-walled carbon nanotubes, *Nano Lett.* 9 (2009) 4338.
- [8] M. Naughton, et al., Efficient nanocoax-based solar cells, *Phys. Status Solidi RRL* 4 (2010) 181.
- [9] C. Chen, R. Jia, H.F. Li, Y.L. Meng, X.Y. Liu, Electrode-contact enhancement in silicon nanowire-array-textured solar cells, *Appl. Phys. Lett.* 98 (2011) 143108.
- [10] B.K. Nayak, V.V. Iyengar, M.C. Gupta, Efficient light trapping in silicon solar cells by ultrafast-laser-induced self-assembled micro/nano structures, *Prog. Photovolt. Res. Appl.* 19 (2011) 631.
- [11] F. Toor, H.M. Branz, M.R. Page, K.M. Jones, H.C. Yuan, Multi-scale surface texture to improve blue response of nanoporous black silicon solar cells, *Appl. Phys. Lett.* 99 (2011) 103501.
- [12] D. Kumar, S.K. Srivastava, P.K. Singh, M. Husain, V. Kumar, Fabrication of silicon nanowire arrays based solar cell with improved performance, *Sol. Energy Mater. Sol. Cells* 95 (2011) 215.
- [13] B.R. Huang, Y.K. Yang, T.C. Lin, W.L. Yang, A simple and low-cost technique for silicon nanowire arrays based solar cells, *Sol. Energy Mater. Sol. Cells* 98 (2012) 357.
- [14] H.J. Syu, S.C. Shiu, Y.J. Hung, C.C. Hsueh, T.C. Lin, T. Subramani, S.L. Lee, C.F. Lin, Influences of silicon nanowire morphology on its electro-optical properties and applications for hybrid solar cells, *Prog. Photovolt. Res. Appl.* 21 (2013) 1400.
- [15] Y.L. Li, H.Y. Yu, J.S. Li, S.M. Wong, X.W. Sun, X.L. Li, C.W. Cheng, H.J. Fan, J. Wang, N. Singh, P.G.Q. Lo, D.L. Kwong, Novel silicon nanohemisphere-array solar cells with enhanced performance, *Small* 7 (2011) 3138.

- [16] H.C. Yuan, V.E. Yost, M.R. Page, P. Stradins, D.L. Meier, H.M. Branz, Efficient black silicon solar cell with a density-graded nanoporous surface: optical properties, performance limitations, and design rules, *Appl. Phys. Lett.* 95 (2009) 123501.
- [17] X. Wang, K.Q. Peng, X.J. Pan, X. Chen, Y. Yang, L. Li, X.M. Meng, W.J. Zhang, S. T. Lee, High-performance silicon nanowire array photoelectrochemical solar cells through surface passivation and modification, *Angew. Chem. Int. Ed.* 50 (2011) 9861.
- [18] J.Y. Kim, M.K. Kwon, V.J. Logeeswaran, S. Grego, M.S. Islam, Postgrowth in situ chlorine passivation for suppressing surface-dominant transport in silicon nanowire devices, *IEEE Trans. Nanotechnol.* 11 (2012) 782.
- [19] X.X. Lin, X. Hua, Z.G. Huang, W.Z. Shen, Realization of high performance silicon nanowire based solar cells with large size, *Nanotechnology* 24 (2012) 235402.
- [20] Z.G. Huang, S.H. Zhong, X. Hua, X.X. Lin, X.Y. Kong, N. Dai, W.Z. Shen, *Prog. Photovolt. Res. Appl.* 23 (2015) 964.
- [21] J. Oh, H.C. Yuan, H.M. Branz, An 18.2%-efficiency black-silicon solar cell achieved through control of carrier recombination in nanostructures, *Nat. Nanotechnol.* 7 (2012) 743.
- [22] S.Y. Liu, X.W. Niu, W. Shan, W. Lu, J.Y. Zheng, Y.F. Li, H.B. Duan, W.J. Quan, W. Z. Han, C.R. Wronski, D.R. Yang, Improvement of conversion efficiency of multicrystalline silicon solar cells by incorporating reactive ion etching texturing, *Sol. Energy Mater. Sol. Cells* 127 (2014) 21.
- [23] S.H. Zhong, B.W. Liu, Y. Xia, J.H. Liu, J. Liu, Z.N. Shen, Z. Xu, C.B. Li, Influence of the texturing structure on the properties of black silicon solar cell, *Sol. Energy Mater. Sol. Cells* 108 (2013) 200.
- [24] G. Xiao, B.W. Liu, J.H. Liu, Z. Xu, The study of defect removal etching of black silicon for solar cells, *Mater. Sci. Semicond. Process.* 22 (2014) 64.
- [25] B.R. Huang, Y.K. Yang, W.L. Yang, Efficiency improvement of silicon nanos-structure based solar cells, *Nanotechnology* 25 (2014) 035401.
- [26] C.H. Lin, D.Z. Dimitrov, C.H. Du, C.W. Lan, Influence of surface structure on the performance of black-silicon solar cell, *Phys. Status Solidi C* 7 (2010) 2778.
- [27] W.Q. Xie, J.I. Oh, W.Z. Shen, Realization of effective light trapping and omni-directional antireflection in smooth surface silicon nanowire arrays, *Nanotechnology* 22 (2011) 065704.
- [28] Y.P. Liu, T. Lai, H.L. Li, Y. Wang, Z.X. Mei, H.L. Liang, Z.L. Li, F.M. Zhang, W. J. Wang, A.Y. Kuznetsov, X.L. Du, Nanostructure formation and passivation of large-area black silicon for solar cell applications, *Small* 8 (2012) 1392.
- [29] W.C. Hsu, Y.S. Lu, J.Y. Chyan, J.A. Yeh, High-efficiency 6" multicrystalline black solar cells based on metal-nanoparticle-assisted chemical etching, *Int. J. Photoenergy* (2012) 197514–2012.
- [30] A.G. Cullis, L.T. Canham, P.D.J. Calcott, The structural and luminescence properties of porous silicon, *J. Appl. Phys.* 82 (1997) 909.
- [31] L. Stalmans, J. Poortmans, H. Bender, M. Caymax, K. Said, E. Vazsonyi, J. Nijs, R. Mertens, Porous silicon in crystalline silicon solar cells: a review and the effect on the internal quantum efficiency, *Prog. Photovolt. Res. Appl.* 6 (1998) 233.
- [32] E. Garnett, P. Yang, Light trapping in silicon nanowire solar cells, *Nano Lett.* 10 (2010) 1082.
- [33] M.D. Kelzenberg, S.W. Boettcher, J.A. Petykiewicz, D.B. Turner-Evans, M. C. Putnam, E.L. Warren, J.M. Spurgeon, R.M. Briggs, N.S. Lewis, H.A. Atwater, Enhanced absorption and carrier collection in Si wire arrays for photovoltaic application, *Nat. Mater.* 9 (2010) 239.
- [34] S.E. Han, G. Chen, Optical absorption enhancement in silicon nanohole arrays for solar photovoltaics, *Nano Lett.* 10 (2010) 1012.
- [35] A.G. Aberle, Surface passivation of crystalline silicon solar cells: a review, *Prog. Photovolt. Res. Appl.* 8 (2000) 473.
- [36] T. Markvart, L. Castaner, *Solar Cells: Materials, Manufacture and Operation*, in: J.W. Liang, et al., (Eds.), Elsevier, Amsterdam, 2009 (Chap. 7).
- [37] M.J. Kerr, A. Cuevas, General parameterization of Auger recombination in crystalline silicon, *J. Appl. Phys.* 91 (2002) 2473.
- [38] Z.N. Shen, B.W. Liu, Y. Xia, J. Liu, J.H. Liu, S.H. Zhong, C.B. Li, Black silicon on emitter diminishes the lateral electric field and enhances the blue response of a solar cell by optimizing depletion region uniformity, *Scr. Mater.* 68 (2013) 199.
- [39] W.J. Yang, Z.Q. Ma, X. Tang, C.B. Feng, W.G. Zhao, P.P. Shi, Internal quantum efficiency for solar cells, *Sol. Energy* 82 (2008) 106.